Geometric Similarities and Topological Phases in Surface Magnon Polaritons

Chen Qian,[1] Jicheng Jin,[1] Thomas Christensen,[2] Li He,[1] Anthony Sigillito,[3] Eugene J. Mele,[1] and Bo Zhen[1,*]
[1]Department of Physics and Astronomy, University of Pennsylvania, Philadelphia, Pennsylvania 19104, USA
[2]Department of Electrical and Photonics Engineering, Technical University of Denmark, Kongens Lyngby 2800, Denmark
[3]Department of Electrical and Systems Engineering, University of Pennsylvania, Philadelphia, Pennsylvania 19104, USA

(Received 21 June 2023; accepted 4 December 2023; published 3 January 2024)

Surface polaritons have proven to be uniquely capable of controlling light-matter interactions. Here we explore surface magnon polaritons in low-loss ferrimagnetic semiconductors, with a focus on their topological phases. We propose several surface magnon polariton devices, including microwave resonators that can strongly enhance magnetic fields and low-loss interconnects joining waveguides with vastly different impedances. Our work can facilitate the exploration of topological phases in polaritons and the development of topological microwave devices for quantum sensing and information processing.

DOI: 10.1103/PhysRevLett.132.013601

The study of topological phases in electromagnetic waves has recently attracted significant attention [1,2]. One intriguing example is the optical quantum anomalous Hall effect [3–5], inspired by Chern insulators of electrons. The bulk topology of these optical systems protects unidirectional transport channels along their edges, which are resilient against backscattering caused by surface roughness or fabrication imperfections. To achieve optical Chern insulators, breaking time-reversal symmetry and electromagnetic reciprocity is crucial. This can be achieved through various means, such as the gyromagnetic effect [6–8] in ferrimagnetic semiconductors, the gyroelectric effect [4] in magnetized plasmas [9,10], or dynamically driving nonlinear materials [11,12]. Notably, gyrotropic effects are prominent at microwave frequencies but significantly weaker at near-infrared and optical frequencies, while optical nonlinearities generally require intense driving fields due to their intrinsic weakness. Additionally, there is growing interest in exploring topological phases in quasiparticle settings, such as polaritons [13–16], which can exist in systems with strong dispersion.

Surface polaritons have proven to be powerful tools for controlling light-matter interactions due to their high spatial squeezing factors. Compared to free-space plane waves at the same frequency, surface polaritons exhibit significantly faster spatial oscillations. While these polaritons are subject to material losses [17], they exhibit a range of fascinating phenomena [18], including strong field enhancements [19], hyperbolic dispersion [20–22], and substantial modifications of nearby emitter dynamics [23], even enabling otherwise forbidden transitions [24–26].

A particularly interesting regime of surface polaritons is the quasistatic limit, characterized by extremely high spatial squeezing factors. In this regime, the electric ($\mathbf{E}$) and magnetic ($\mathbf{B}$) fields of electromagnetic waves are largely decoupled, allowing independent and versatile control over both fields. Two types of materials with negative permittivity, $\epsilon(\omega) < 0$, have garnered significant attention: metals below their plasma frequencies [27–30] (together with indium tin oxide [31] and gaseous-phase plasma) and polar crystals within their reststrahlen bands [32]. Alternatively, materials with negative permeability, $\mu(\omega) < 0$, such as those near ferromagnetic resonances in ferrites [33], can also be utilized, although this approach has received less focus.

This work studies surface magnon polaritons (SMP) in ferrite structures and identifies a Chern insulator topological phase in an array of SMP ring resonators. We present a universal method to geometrically scale SMP structures in the quasimagnetostatic limit, which enables easy adjustment of their energy velocity [34] and effective impedance while maintaining their frequencies. This geometric scaling technique is further applied to the SMP Chern insulators and their chiral edge states to develop a compact and lossless interconnect between waveguides with vastly different impedances. This work paves the way for future exploration of new methods to localize magnetic fields at microwave frequencies for quantum applications and the development of topological microwave devices.

We start by introducing the geometric scaling rule for electromagnetic waves in the quasistatic limit before applying it to different SMP structures in conventional and topological settings. There exists a class of solutions to Maxwell's equations where the spatial oscillation is significantly faster than the temporal oscillation ($k \gg \omega/c$). One such example is known as the surface polaritons, which arise at the interfaces between air and materials with negative permittivity ε (e.g., surface plasmon polaritons [29,35] and surface phonon polaritons [36]) or negative permeability μ (surface magnon polaritons). In strongly localized surface plasmon polaritons (surface magnon polaritons), the magnetic (electric) field strength is nearly

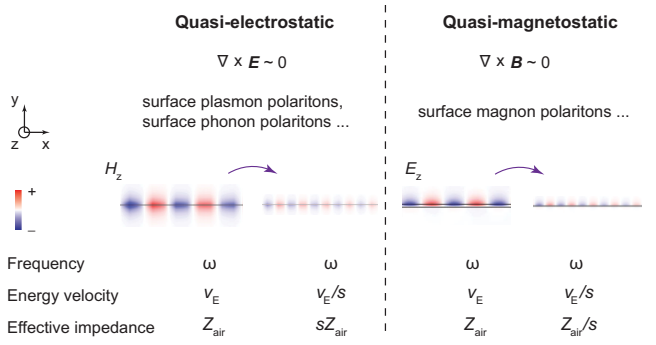

FIG. 1. Geometric scaling of electromagnetic waves in quasistatic settings. Geometrically scaling down a surface polariton waveguide, in the quasielectrostatic or quasimagnetostatic limit, provides an effective method to adjust the energy velocity and the effective impedance, while maintaining the same operational frequency.

zero, $\mathbf{B} \propto \mathbf{H} \sim \mathbf{0}$ ($\mathbf{D} \propto \mathbf{E} \sim \mathbf{0}$). To satisfy Faraday's law, $\nabla \times \mathbf{E} = -\partial \mathbf{B}/\partial t$ (Ampere-Maxwell equation, $\nabla \times \mathbf{H} = \partial \mathbf{D}/\partial t$), the left-hand side of the equation also needs to vanish. Namely, the electric (magnetic) field needs to be nearly curl free, akin to the electrostatic (magnetostatic) limit.

In both quasistatic limits (Fig. 1), the electric and magnetic fields are effectively decoupled, allowing them to vary independently under scaling transformations. For instance, when a polaritonic waveguide in the quasielectrostatic limit is scaled down by a factor of s, the operating frequency ω remains unchanged. Meanwhile, the $\mathbf{E}$ field is increased by a factor of s while the $\mathbf{H}$ field remains nearly unchanged. On the other hand, in quasimagnetostatics, the same scaling down operation will increase the $\mathbf{H}$ field by a factor of s while keeping the $\mathbf{E}$ field unchanged. In both cases, the energy velocity v_E is reduced by a factor of s.

Motivated by these insights, we proceed to derive the dispersions of surface-magnon polariton (SMP) waveguides and examine their behavior under geometric scaling. A typical SMP waveguide configuration involves a ferrimagnetic semiconductor, such as the yttrium iron garnet (YIG), with a finite width. The waveguide is subjected to an external magnetic field, $B_{\text{ext}}\hat{\mathbf{z}}$, oriented tangentially to the surfaces of the waveguide, which is assumed to lie in the xz plane [Fig. 2(a)]. The magnetic permeability tensor of YIG reads as

$$\boldsymbol{\mu} = \boldsymbol{\eta} \begin{pmatrix} \mu_+ & & \\ & \mu_- & \\ & & \mu_0 \end{pmatrix} \boldsymbol{\eta}^\dagger, \quad \boldsymbol{\eta} = \begin{pmatrix} \frac{1}{\sqrt{2}} & \frac{\mathrm{i}}{\sqrt{2}} & \\ \frac{\mathrm{i}}{\sqrt{2}} & \frac{1}{\sqrt{2}} & \\ & & 1 \end{pmatrix}. \quad (1)$$

Here the column vectors of the unitary matrix $\boldsymbol{\eta}$ correspond to the optical principle axes $\hat{\mathbf{e}}_\pm = (\hat{\mathbf{x}} \pm \mathrm{i}\hat{\mathbf{y}})/\sqrt{2}$ and $\hat{\mathbf{e}}_3 = \hat{\mathbf{z}}$ of the magnetized YIG material. Along principal axes $\hat{\mathbf{e}}_\pm$, the effective permeability reads as

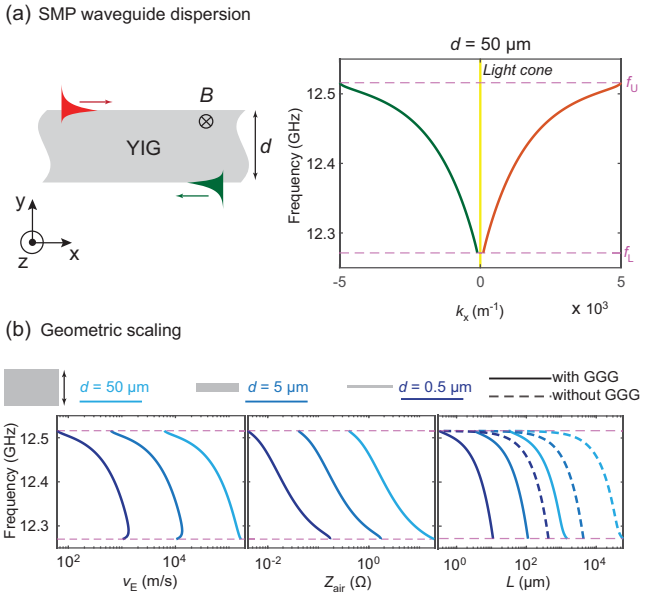

FIG. 2. SMP waveguide dispersion and geometric scaling. (a) Schematic drawing of a SMP waveguide based on ferrimagnetic semiconductors (YIG) placed in an external magnetic field. The two SMP waveguide modes (red and green) live on opposite surfaces and travel in opposite directions. (b) Scaling down the waveguide width d by factors of $s = 10$, from 50 to 5 and then to 0.5 μm, results in a proportional decrease in the energy velocity v_E, effective impedance Z_{air}, and propagation length L. Solid (dashed) lines in the last panel are calculated when a GGG substrate is (not) used, causing a higher (lower) material loss.

$$\mu_\pm = \mu_0(1 + \chi_\pm) = \mu_0\left[1 + \frac{f_M}{(f_H \pm f) + \mathrm{i}\alpha f}\right]. \quad (2)$$

Here $f = \omega/2\pi$ is the frequency, $f_H = \gamma_0 H$, and $f_M = \gamma_0 M$, where γ_0 is the gyromagnetic ratio of YIG (2.8 MHz/Oe). The external magnetic field is denoted as $H = B_{\text{ext}}/\mu_0 = 3570$ Oe, and the magnetization of YIG is taken to be $M = 1800$ Oe, following Refs. [37] and [38]. The Gilbert damping constant is taken to be $\alpha = 8.9 \times 10^{-4}$, which is consistent with experimental results when a gadolinium gallium garnet (GGG) substrate is used [39–41]. Removing the GGG substrate can substantially reduce the damping [39] and facilitate a much longer propagation length [dashed lines in Fig. 2(b)]. For our 2D calculations, the demagnetization field [37,42] is zero since the sample extends to infinity in the direction of the external magnetic field. See the Supplemental Material [43] for more details of the material properties.

Besides electromagnetic modes that extend through the bulk, localized SMP modes are found at the interfaces between YIG and air [Fig. 2(a)], which are also known as magnetostatic surface waves (MSSW) in the literature. Unlike the conventional MSSW results derived under the magnetostatic approximation ($\mathbf{E} = \mathbf{0}$), we solve the full Maxwell's equations without such approximations, leading

to several deviations in their dispersions as explained below. The SMP waveguide modes are bound in frequency: between a lower limit $f_L = \sqrt{f_H(f_H + f_M)}$ and an upper limit $f_U = f_H + f_M/2$. The lower limit f_L, often denoted as $f_\perp$ in the MSSW literature, represents the resonance frequency of a forward volume wave with a magnetic field polarized perpendicular to the external magnetic field ($\mathbf{B} \perp \mathbf{B}_{ext}$). We note that the upper limit f_U is defined under the assumption of lossless materials. Consequently, it may appear that this limit is exceeded in our results, which is due to our calculations incorporating realistic material losses.

Our calculated SMP dispersion starts from a finite momentum at the lower frequency bound f_L, unlike the MSSW results derived under the magnetostatic approximation where it starts from zero momentum [42,47]. The SMP dispersion consists of two branches: one (red curve) localized on the upper interface and traveling to the right, and the other (green curve) localized on the bottom interface and traveling to the left. These waveguide modes exhibit nonreciprocal behavior due to the broken time-reversal symmetry and reciprocity caused by the YIG permeability. The SMP dispersion exhibits a symmetry $\omega(k_x) = \omega(-k_x)$ due to the C_2^z symmetry of the waveguide. The momentum of both SMP branches, $k_x \sim 10^3$ m^{-1}, is significantly larger than that of free-space modes at the same frequencies ($f/c \sim 40$ m^{-1}), confirming the quasi-magnetostatic nature of the SMP modes.

To validate the scaling rules of SMP modes, we geometrically scale SMP waveguides to different widths (d): as d is decreased by factors of $s = 10$, from 50 μm to 5 μm to 0.5 μm, the frequency range of SMP remains unchanged; however, the in-plane momentum k_x increases by factors of 10 [Fig. 2(b)]. This is consistent with the predicted scaling rules. Accordingly, the energy velocity v_E, effective impedance in the air Z_{air}, and propagation length L also decrease by factors of $s = 10$.

SMP resonators can also be constructed by curving the SMP waveguide into a ring resonator, characterized by inner radius r_i, outer radius r_o, and width $d = r_o - r_i$ [Fig. 3(a)]. The rotational symmetry of the ring resonator leads to the quantization of SMP resonances based on their azimuthal numbers m: $\mathbf{E}_z^m \propto e^{im\phi}$. Here ϕ represents the polar angle in cylindrical coordinates. Nonreciprocal behaviors similar to those of the waveguide modes are also observed in SMP resonances: resonances with $m > 0$ (red circles) localize at the inner surface of the ring and propagate in the counterclockwise direction, while those with $m < 0$ (green circles) localize at the outer surface and propagate in the clockwise direction. The frequencies of SMP resonances (circles) are in good agreement with the SMP waveguide dispersion (dashed lines) when the momentum of the SMP resonance is associated with the azimuthal number m according to $k = m/r_{eff}$, where $r_{eff} = d/\ln(r_o/r_i)$. This relationship is demonstrated in Fig. 2(a), through an example with $d = 50$ μm and

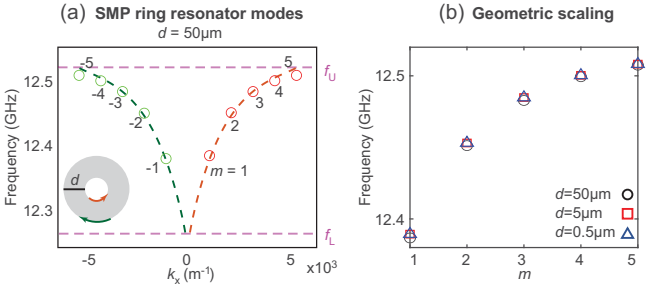

FIG. 3. SMP ring resonators and scaling invariance. (a) SMP ring resonators support two sets of resonances, labeled by positive and negative azimuthal numbers m, that propagate on opposite surfaces and in opposite directions. The SMP resonance frequencies agree well with the SMP waveguide dispersion with the same width d. (b) Geometrically scaling down the ring resonators by factors of $s = 10$ does not alter the resonance frequencies.

$r_i = 120$ μm. See the Supplemental Material [43] for more details. The SMP resonance frequency increases with the absolute value of m. Our calculations reveal that SMP resonances with opposite m values are very close in frequency, although they are not identical as previously noted in the MSSW literature [42,47].

The geometric scaling behavior is also observed in SMP ring resonances [Fig. 3(b)]. When the entire structure is scaled down by a factor of 10 (or 100), the new SMP resonance frequencies labeled by red squares (or blue triangles) remain nearly identical to their original values, labeled as black circles.

Beyond the conventional devices discussed earlier, topological devices can be constructed by arranging SMP ring resonators into a square lattice array, as illustrated in Fig. 4(a). Each ring here is identical to the one depicted in Fig. 3(b), with a width of $d = 5$ μm. When the lattice constant is set to be $a = 108$ μm, the rings are sufficiently far apart. Consequently, the band structure is predominantly composed of nearly flat bands, which result from individual ring resonator modes with opposite m values (such as $m = \pm 2$ or $m = \pm 3$). However, there are three highly dispersive bands that are primarily constituted by the $m = 0$ and $m = \pm 1$ modes. Interestingly, many of the resulting SMP energy gaps exhibit nontrivial topology, as evidenced by nonzero Chern numbers (e.g., $C = 1$). This observation aligns with the analysis of C_2^z indices of the eigenmodes at high symmetry points (Γ and M) in the band structure, as detailed in the Supplemental Material [43].

To confirm the Chern insulator nature of the SMP energy gaps, a supercell geometry is employed to examine the presence of chiral edge states (CES) between the SMP ring resonator array and a perfect electric conductor (PEC), as shown in Fig. 4(b). Indeed, pairs of CESs are observed between 12.397 and 12.452 GHz, as well as between 12.455 and 12.483 GHz. These pairs of CESs, denoted by red and blue lines, localize at opposite interfaces

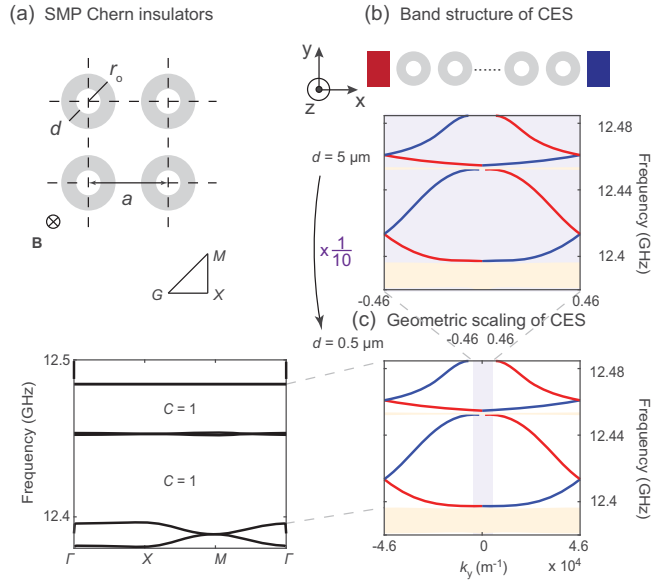

FIG. 4. SMP Chern insulators and geometric scaling of chiral edge states. (a) Schematics of a SMP Chern insulator consisting of a square lattice of SMP ring resonators. The band structure exhibits topological gaps with nonzero Chern numbers ($C = 1$). (b) Simulation results confirm the bulk topology, showing CES at the interfaces between the SMP Chern insulator and perfect electric conductors. (c) Owing to geometric similarities, scaling down the SMP Chern insulator by a factor of $s = 10$ keeps the CES frequency unchanged but increases their momenta k_y by a factor of $s = 10$.

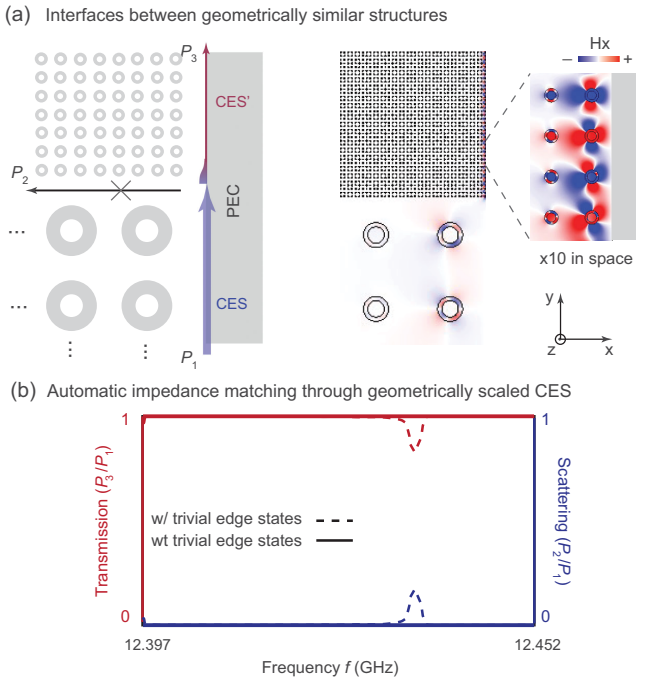

FIG. 5. Topological interconnect between SMP waveguides of different impedance. (a) Schematic of an interconnect between an SMP CES (blue arrow) and its geometrically scaled-down version (CES′, purple arrow). (b) When trivial edge states (P_2) are eliminated by engineering the interface, all input power is transmitted through ($P_3/P_1 = 1$, solid line), despite the orders of magnitude difference between the impedance of the input and output waveguides (CES). When trivial edge states are present, scattering becomes allowed, and the transmission is no longer perfect (dashed lines).

(left and right) and propagate in opposite directions (downward and upward). We note that compared to previous photonic Chern insulators that also utilize YIG [3,6,7], our unit cells and feature sizes are approximately 2–3 orders of magnitude smaller, which confirms the high spatial squeezing factors of SMP. We also note that due to the high spatial squeezing factors, the effective medium theory does not generally apply to the SMP, particularly in the magnetostatic regime. Finally, most of the CES lies below the light line and may not require confinement from PECs in practice.

Both the SMP Chern insulator and CES can be geometrically scaled. When the unit cell is reduced by a factor of $s = 10$, resulting in a decrease of d from 5 μm to 0.5 μm and a decrease of a from 108 μm to 10.8 μm, the Chern numbers of the bands and the frequencies of the CESs remain unchanged [Fig. 4(c)], but now with 10 times the momentum k_y. Consequently, the CES energy velocity v_E and the effective impedance Z_{air} are also reduced by factors of $s = 10$.

A compact and lossless interconnect can be created between geometrically similar CES. The configuration [Fig. 5(a)] involves placing an SMP Chern insulator (bottom section) adjacent to a scaled-down version ($s = 20$) of itself (top section). Both structures are terminated by PECs on the right side. When power P_1 is input through the bottom CES (blue arrow), backscattering is prohibited due to the unidirectionality of the CES. Consequently, it can only be transmitted through its geometrically scaled-down counterpart (purple arrow toward the top, P_3), or it can be scattered through possible trivial edge states (gray arrow toward the left, P_2). By engineering the interface between the two Chern insulators with identical Chern numbers, one can eliminate such trivial edge states [43]. This ensures that all input power is transmitted through, with P_3/P_1 being 1 [Fig. 5(b)]. This is achieved despite a significant mismatch in energy velocity and effective impedance between the input and output CES. The ability to change the effective impedance by orders of magnitude while maintaining a consistent frequency range is a distinctive characteristic of quasistatic systems, such as SMP. Such adjustments cannot be straightforwardly implemented in dynamic systems, such as gyromagnetic photonic crystals [3,43].

The structures we proposed are practically feasible for fabrication and testing. While our calculations here focus on 2D structures, similar results can be achieved in 3D structures defined in thin-film YIG placed between metallic plates, as demonstrated in previous experimental

works [6,7]. Commercially available thin-film YIG wafers with narrow ferromagnetic resonance linewidths [38] are well-suited for these implementations. Furthermore, the proposed structures, such as waveguides and ring resonators, can be fabricated using standard etching techniques described in existing literature [48,49].

The geometric scaling rules presented here only apply to certain parameter regimes. For example, overly wide waveguides (with $d \gg 100$ μm) fail to achieve the spatial confinement necessary for operation in the quasimagnetostatic limit, which results in the SMP dispersion being unresponsive to variations in waveguide width. On the other hand, overly narrow waveguides (with $d \ll 1$ μm) necessitate accounting for the magnetic dipole exchange interaction, an aspect not included in our calculations. Further investigation of such fine structures could delve into the exchange regime of electromagnetic waves [50,51], potentially revealing more complex and intriguing phenomena.

In summary, this work studies SMP devices in ferrimagnetic semiconductors and their topological properties. The proposed geometric scaling rules enable easy adjustments of light speed and effective impedance in the quasimagnetostatic limit. Our findings open up avenues for exploring topological phases in polaritonic systems, manipulating magnetic fields in the microwave regime, and designing robust and compact topological microwave devices.

The authors acknowledge stimulating conversations with Nicholas Rivera, Jamison Sloan, and Marin Soljačić. This work was partly supported by the U.S. Office of Naval Research (ONR) through Grant No. N00014-20-1-2325 on Robust Photonic Materials with High-Order Topological Protection and Grant No. N00014-21-1-2703, the Air Force Office of Scientific Research through Grant No. FA9550-21-1-0299. Work by T. C. is supported by a research grant (Project No. 42106) from Villum Fonden. Work by E. J. M. is supported by the Department of Energy under Grant No. DE-FG02-84ER45118.

*bozhen@sas.upenn.edu

[1] T. Ozawa, H. M. Price, A. Amo, N. Goldman, M. Hafezi, L. Lu, M. C. Rechtsman, D. Schuster, J. Simon, O. Zilberberg *et al.*, Topological photonics, Rev. Mod. Phys. **91**, 015006 (2019).

[2] L. Lu, J. D. Joannopoulos, and M. Soljačić, Topological photonics, Nat. Photonics **8**, 821 (2014).

[3] Z. Wang, Y. D. Chong, J. D. Joannopoulos, and M. Soljačić, Reflection-free one-way edge modes in a gyromagnetic photonic crystal, Phys. Rev. Lett. **100**, 013905 (2008).

[4] F. D. M. Haldane and S. Raghu, Possible realization of directional optical waveguides in photonic crystals with broken time-reversal symmetry, Phys. Rev. Lett. **100**, 013904 (2008).

[5] M. C. Rechtsman, J. M. Zeuner, Y. Plotnik, Y. Lumer, D. Podolsky, F. Dreisow, S. Nolte, M. Segev, and A. Szameit, Photonic Floquet topological insulators, Nature (London) **496**, 196 (2013).

[6] Z. Wang, Y. Chong, J. D. Joannopoulos, and M. Soljačić, Observation of unidirectional backscattering-immune topological electromagnetic states, Nature (London) **461**, 772 (2009).

[7] S. A. Skirlo, L. Lu, Y. Igarashi, Q. Yan, J. Joannopoulos, and M. Soljačić, Experimental observation of large Chern numbers in photonic crystals, Phys. Rev. Lett. **115**, 253901 (2015).

[8] B. Bahari, A. Ndao, F. Vallini, A. El Amili, Y. Fainman, and B. Kanté, Nonreciprocal lasing in topological cavities of arbitrary geometries, Science **358**, 636 (2017).

[9] F. R. Prudêncio and M. G. Silveirinha, Ill-defined topological phases in local dispersive photonic crystals, Phys. Rev. Lett. **129**, 133903 (2022).

[10] C. Qian, Y. Jiang, J. Jin, T. Christensen, M. Soljačić, A. V. Kildishev, and B. Zhen, Topological electromagnetic waves in dispersive and lossy plasma crystals, Sci. Rep. **13**, 20445 (2023).

[11] L. He, Z. Addison, J. Jin, E. J. Mele, S. G. Johnson, and B. Zhen, Floquet Chern insulators of light, Nat. Commun. **10**, 4194 (2019).

[12] K. Fang and Y. Wang, Anomalous quantum Hall effect of light in Bloch-wave modulated photonic crystals, Phys. Rev. Lett. **122**, 233904 (2019).

[13] D. Basov, M. Fogler, and F. García de Abajo, Polaritons in van der Waals materials, Science **354**, aag1992 (2016).

[14] L. He, J. Wu, J. Jin, E. J. Mele, and B. Zhen, Polaritonic Chern insulators in monolayer semiconductors, Phys. Rev. Lett. **130**, 043801 (2023).

[15] T. Karzig, C.-E. Bardyn, N. H. Lindner, and G. Refael, Topological polaritons, Phys. Rev. X **5**, 031001 (2015).

[16] W. Liu, Z. Ji, Y. Wang, G. Modi, M. Hwang, B. Zheng, V. J. Sorger, A. Pan, and R. Agarwal, Generation of helical topological exciton-polaritons, Science **370**, 600 (2020).

[17] J. B. Khurgin, How to deal with the loss in plasmonics and metamaterials, Nat. Nanotechnol. **10**, 2 (2015).

[18] D. N. Basov, A. Asenjo-Garcia, P. J. Schuck, X. Zhu, and A. Rubio, Polariton panorama, Nanophotonics **10**, 549 (2020).

[19] F. H. Jornada, L. Xian, A. Rubio, and S. G. Louie, Universal slow plasmons and giant field enhancement in atomically thin quasi-two-dimensional metals, Nat. Commun. **11**, 1013 (2020).

[20] Y. Yang, P. Qin, X. Lin, E. Li, Z. Wang, B. Zhang, and H. Chen, Type-I hyperbolic metasurfaces for highly-squeezed designer polaritons with negative group velocity, Nat. Commun. **10**, 2002 (2019).

[21] G. Hu, W. Ma, D. Hu, J. Wu, C. Zheng, K. Liu, X. Zhang, X. Ni, J. Chen, X. Zhang *et al.*, Real-space nanoimaging of hyperbolic shear polaritons in a monoclinic crystal, Nat. Nanotechnol. **18**, 64 (2022).

[22] N. C. Passler, X. Ni, G. Hu, J. R. Matson, G. Carini, M. Wolf, M. Schubert, A. Alù, J. D. Caldwell, T. G. Folland *et al.*, Hyperbolic shear polaritons in low-symmetry crystals, Nature (London) **602**, 595 (2022).

[23] A. Tiene, J. Levinsen, M. M. Parish, A. H. MacDonald, J. Keeling, and F. M. Marchetti, Extremely imbalanced

two-dimensional electron-hole-photon systems, Phys. Rev. Res. **2**, 023089 (2020).
[24] N. Rivera, I. Kaminer, B. Zhen, J. D. Joannopoulos, and M. Soljačić, Shrinking light to allow forbidden transitions on the atomic scale, Science **353**, 263 (2016).
[25] N. Rivera and I. Kaminer, Light–matter interactions with photonic quasiparticles, Nat. Rev. Phys. **2**, 538 (2020).
[26] J. Sloan, N. Rivera, J. D. Joannopoulos, I. Kaminer, and M. Soljačić, Controlling spins with surface magnon polaritons, Phys. Rev. B **100**, 235453 (2019).
[27] H. Reather, Surface plasmons on smooth and rough surfaces and on gratings, Springer Tracts Mod. Phys. **111**, 345 (1988).
[28] A. V. Zayats, I. I. Smolyaninov, and A. A. Maradudin, Nano-optics of surface plasmon polaritons, Phys. Rep. **408**, 131 (2005).
[29] A. N. Grigorenko, M. Polini, and K. Novoselov, Graphene plasmonics, Nat. Photonics **6**, 749 (2012).
[30] F. J. García de Abajo, Graphene plasmonics: Challenges and opportunities, ACS Photonics **1**, 135 (2014).
[31] P. R. West, S. Ishii, G. V. Naik, N. K. Emani, V. M. Shalaev, and A. Boltasseva, Searching for better plasmonic materials, Laser Photonics Rev. **4**, 795 (2010).
[32] E. Palik, History of far-infrared research. I. The Rubens era, J. Opt. Soc. Am. **67**, 857 (1977).
[33] A. B. Fuller, *Ferrites at Microwave Frequencies* (IET, London, 1987), Vol. 23.
[34] O. B. Vorobyev, Energy density and velocity of electromagnetic waves in lossy chiral medium, J. Opt. **16**, 015701 (2017).
[35] M. Jablan, H. Buljan, and M. Soljačić, Plasmonics in graphene at infrared frequencies, Phys. Rev. B **80**, 245435 (2009).
[36] J. D. Caldwell, L. Lindsay, V. Giannini, I. Vurgaftman, T. L. Reinecke, S. A. Maier, and O. J. Glembocki, Low-loss, infrared and terahertz nanophotonics using surface phonon polaritons, Nanophotonics **4**, 44 (2015).
[37] D. M. Pozar, *Microwave Engineering*, 4th ed. (Wiley, New York, 2011).
[38] C. Dubs, O. Surzhenko, R. Linke, A. Danilewsky, U. Brückner, and J. Dellith, Sub-micrometer yttrium iron garnet LPE films with low ferromagnetic resonance losses, J. Phys. D **50**, 204005 (2017).
[39] S. Kosen, A. F. van Loo, D. A. Bozhko, L. Mihalceanu, and A. D. Karenowska, Microwave magnon damping in YIG films at millikelvin temperatures, APL Mater. **7**, 101120 (2019).
[40] C. L. Jermain, S. V. Aradhya, N. D. Reynolds, R. A. Buhrman, J. T. Brangham, M. R. Page, P. C. Hammel, F. Y. Yang, and D. C. Ralph, Increased low-temperature damping in yttrium iron garnet thin films, Phys. Rev. B **95**, 174411 (2017).
[41] P. Pirro, V. I. Vasyuchka, A. A. Serga, and B. Hillebrands, Advances in coherent magnonics, Nat. Rev. Mater. **6**, 1114 (2021).
[42] A. G. Gurevich and G. A. Melkov, *Magnetization Oscillations and Waves* (CRC Press, Boca Raton, 1996).
[43] See Supplemental Material at http://link.aps.org/supplemental/10.1103/PhysRevLett.132.013601 for more details on material properties of YIG, SMP ring resonator effective radius, SMP Chern insulator topology, trivial edge state engineering, and the comparison between Chern insulators which includes Refs. [3,39,40,44–46].
[44] H. How, P. Shi, C. Vittoria, L. C. Kempel, and K. D. Trott, Single-crystal YIG phase shifter using composite stripline structure at *X* band, J. Appl. Phys. **87**, 4966 (2000).
[45] X. Zhang, C. Zou, L. Jiang, and H. X. Tang, Superstrong coupling of thin film magnetostatic waves with microwave cavity, J. Appl. Phys. **119**, 023905 (2016).
[46] C. Fang, M. J. Gilbert, and B. A. Bernevig, Bulk topological invariants in noninteracting point group symmetric insulators, Phys. Rev. B **86**, 115112 (2012).
[47] D. D. Stancil, *Theory of Magnetostatic Waves* (Springer Science & Business Media, New York, 2012).
[48] A. V. Chumak *et al.*, Advances in magnetics roadmap on spin-wave computing, IEEE Trans. Magn. **58**, 1 (2022).
[49] N. Zhu, X. Zhang, X. Han, C.-L. Zou, and H. X. Tang, Inverse Faraday effect in an optomagnonic waveguide, Phys. Rev. Appl. **18**, 024046 (2022).
[50] L. J. Cornelissen, K. Oyanagi, T. Kikkawa, Z. Qiu, T. Kuschel, G. E. W. Bauer, B. J. van Wees, and E. Saitoh, Nonlocal magnon-polaron transport in yttrium iron garnet, Phys. Rev. B **96**, 104441 (2017).
[51] Y. Yang, D. Zhu, W. Yan, A. Agarwal, M. Zheng, J. D. Joannopoulos, P. Lalanne, T. Christensen, K. K. Berggren, and M. Soljačić, A general theoretical and experimental framework for nanoscale electromagnetism, Nature (London) **576**, 248 (2019).